Renewable Energy 228 (2024) 120653

Contents lists available at ScienceDirect

Renewable Energy

journal homepage: www.elsevier.com/locate/renene

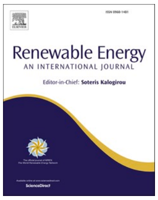

A Full-Scale Tidal Blade Fatigue Test using the FastBlade Facility

Sergio Lopez Dubon [a,*], Christopher Vogel [b], David Garcia Cava [a], Fergus Cuthill [a], Edward D. McCarthy [a], Conchur M. Ó Bradaigh [c]

[a] *School of Engineering, The University of Edinburgh Edinburgh, Scotland, United Kingdom*
[b] *Department of Engineering Science, University of Oxford Oxford, England, United Kingdom*
[c] *Faculty of Engineering, The University of Sheffield, Sheffield, S10 2TN, England, United Kingdom*

ARTICLE INFO

Keywords:
Testing
Fatigue
Tidal steam blades
Composites

ABSTRACT

Fatigue testing of tidal turbine blades requires the application of cyclic loads without the ability to match the natural frequency of the blade due to their high stiffness and the associated thermal issues of testing composite materials at those frequencies (i.e., 18–20 Hz). To solve this, loading the blades with an auxiliary system is necessary; in most cases, a conventional hydraulic system tends to be highly energy-demanding and inefficient. A regenerative digital displacement hydraulic pump system was employed in the FastBlade fatigue testing facility, which saved up to 75 % compared to a standard hydraulic system. A series of equivalent target loads were defined using Reynolds-Averaged Navier Stokes (RANS) simulations (based on on-site collected water velocity data) and utilised in FastBlade to demonstrate an efficient way to perform fatigue testing. During the test, a series of measurements were performed on the blade response and the Fastblade test structure itself, providing novel insights into the mechanical behaviour of a blade, and enabling improved testing practice for FastBlade. Without catastrophic failure, the blade withstood the principal tidal loading for 20 years (equivalent). This test data will enable FastBlade to identify improvements to the testing procedures, i.e., control strategies, load introduction, instrumentation layout, instrument calibration, and test design.

1. Introduction

1.1. *Tidal energy sector and current scenario for tidal turbine blade design*

It is projected that tidal and wave sources could contribute 100 GW to the EU power grid by 2050, powering a third of homes and adding €140 bn of economic activity and ca. 500,000 jobs in Europe alone [1]. Globally, 150–800 TWh (terawatt hours) or EUR 40 billion per year of activity is projected [2]. Tidal stream energy is a key sector contributing to this growth, and horizontal axis turbines (HATs) are the underpinning technology. Much of the supporting technology and design methodology for HATs have been adapted from the wind turbine sector. Mapping designs and methodologies from wind turbine blades to tidal turbine blades presents challenges due to the distinct operating environments. Tidal turbines function in seawater 800 times denser than air, leading to substantially higher and more complex loads (i.e., higher turbulence effects) compared to those that a specimen of the same length experiment due to the air action. Consequently, direct translation of wind turbine designs and methodologies isn't feasible due to the unique demands posed by the denser medium of seawater. Preliminary design of tidal turbine blades based on blade element momentum theory and simplified Finite Element Models of composite blades are given for static loading in Ref. [3] and for design life calculations in Refs. [4,5].

Tidal turbine blades are much shorter than the largest offshore wind blades (e.g., 6–8 m v. 100 m plus), since they operate in a medium ca. 800 times denser. Secondly, to manage the higher fluid stresses, they can have blade root sections with wall thickness ca. 100 mm, compared with tip thicknesses ca. 6–10 mm [6]. This means that the transition from the blade root to tip occurs rapidly over the length of the blade, which tends to create stress concentrations over the root-to-body transition zone. These high-stress concentrations, in turn, create an elevated risk of fatigue failure over the 20-year design life of a typical blade.

Currently, there are insufficient data and understanding of fatigue in tidal blades, which is one of the reasons that tidal stream energy retains a relatively high levelised cost of energy (LCOE) compared with other renewable energy technologies. Cost of energy is expected to fall as more tidal turbines are built with significant learning and innovations to follow, in a similar fashion to offshore wind. In 2022, four tidal

---

* Corresponding author.
E-mail address: Sergio.LDubon@ed.ac.uk (S. Lopez Dubon).

https://doi.org/10.1016/j.renene.2024.120653
Received 17 March 2023; Received in revised form 27 February 2024; Accepted 13 May 2024

companies were awarded UK Contracts for Difference of £178/MWh, which is high compared to the current LCOE of £37.35/MWh for offshore wind projects [7]. This has led to a renewed focus on improved test methods, more representative data, and a new design methodology to radically reduce turbine blade fatigue failure risk.

In recent years, several advances have been made in full-scale fatigue testing of composite material tidal blades. These include the test performed in 2018 by Ref. [8] in the Large Structure Laboratory of the University of Galway, where a 3/8th scaled-down blade design by OpenHydro was tested. The test was performed using a servo-hydraulic actuator system, achieving a maximum load amplitude of 35 kN and 275,000 cycles.

Later, in 2020, a new turbine blade fatigue test standard was published, IEC TS 62600–3:2020 [9], which codifies a test method for fatigue testing of full-scale tidal blades, and in 2022, the new FastBlade facility at Port of Rosyth, Scotland, was opened, which has the capability to deliver accelerated lifetime fatigue testing of a full-scale tidal blade and other long slender structures [10]. These two developments enabled this Supergen ORE Hub LoadTide project, the first project to achieve accelerated lifetime fatigue testing of a tidal turbine blade.

Also in 2022, at at the University of Galway, another fatigue test was performed [11] with two full-scale blades of 2 and 3 m in length from SCHOTTEL HYDRO. The test campaign consisted of natural frequency, static, fatigue and residual strength testing. For the fatigue test of the 2-m blade, a maximum load of 6.9 kN was achieved during 150,000 cycles at 0.3Hz; and for the 3-m blade, a maximum load of 14 kN was reached during 16,000 cycles at 0.1Hz.

In this paper, we show how FastBlade is the first test facility globally capable of delivering a high load during the fatigue testing of a tidal blade, performing 31,775 cycles at 1 Hz with a target load of 183.7 kN, making such a test economic for the first time. The facility is enabled by a unique pumping system that features regenerative pumping and digital displacement hydraulics [12–14]. The combination of these features can reduce effective testing energy by up to 75 %, thus enabling testing to be delivered in several weeks rather than months; this renders such testing economic for blade developers. This paper describes the first tidal turbine blade test conducted in FastBlade in the Summer of 2022, which generated fatigue performance data for a previously deployed tidal turbine blade installed on a tidal stream turbine at Fall of Warness, Orkney, Scotland, UK.

2. Methods

2.1. Site data

The flow data used in this project were sourced from the ReDAPT project at the Fall of Warness, European Marine Energy Centre (EMEC), Orkney UK [15–17]. The data was collected using two acoustic Doppler current profilers deployed between 19 July and August 2, 2013. The profilers were positioned 0.8 m above the seabed and sampled the flow at a frequency of 0.5 Hz. The mean operating depth of the profilers during deployment was 43.2 m and 46.2 m due to the slightly different seabed conditions at their respective locations.

Flow speed and turbulence intensity data were binned into hub-height mean flow speed bins of $U_\infty = (0.7, 1.4, 2.1, 2.8, 3.0, 3.5)$ m s^{-1} for both the flood and ebb tides, noting that $U_\infty = 3.5$ m s^{-1} was only achieved during the ebb tide. Data was only included if the wave height was less than 1 m. The ensemble length for all statistics was 5 min, and a 0.12 cm s^{-1} noise correction estimate was made to the turbulence intensity data following [16].

Vertical profiles of flow speed and turbulence intensity are presented in Fig. 1, demonstrating the differences in the simulated profiles between the ebb and flood tides. A slight reduction in flow speed near the surface during the ebb tides arises because the flow is funnelled around the islands surrounding the Falls of Warness site. A consequence of this is that the fastest flows were encountered about halfway through the water column at the highest flow speed bins. This also gives rise to the differences in the turbulence intensity profiles between the flood and ebb tides. Consequently, the standard deviation of the flow speed across the rotor plane is consistently higher for flood tides than the ebb tides for a specified hub-height flow speed, as shown in Ref. [16].

During the flood tide, the velocity profiles follow an approximately 1/6th power law, whereas this is closer to a 1/5th power law for the ebb tide in the lower portion of the flow, which is unaffected by the near-surface flow speed reduction present in the Falls of Warness described above.

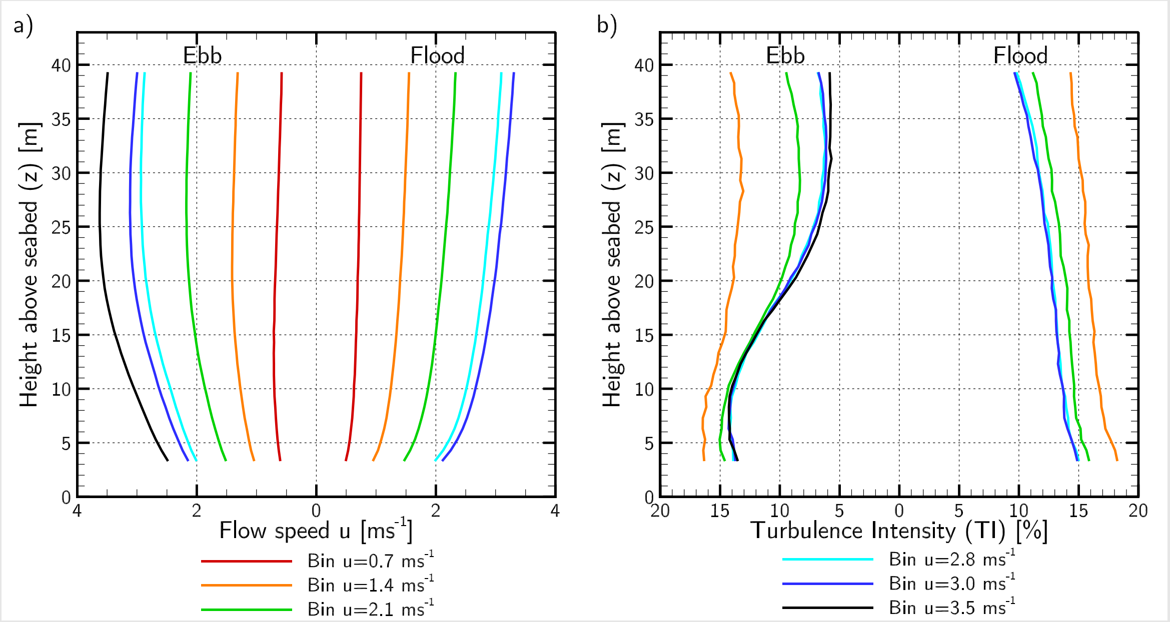

Fig. 1. *Simulated vertical profiles of (a) flow speed (u) and (b) turbulence intensity (TI) at the Fall of Warness ReDAPT site, based on* [16]. *Data binned by hub-height mean velocity for ebb and flood tide conditions. The turbine hub height is 19 m.*

2.2. Computational model

A suite of unsteady Reynolds-Averaged Navier Stokes (URANS) simulations were performed using the computational fluid dynamics (CFD) solver OpenFOAM (version 2.3.1). The choice of URANS simulation draws on the work of Ahmed et al., which found that URANS and Large Eddy Simulation predict very similar phase-averaged loads and blade pressure distributions in low onset turbulence flows [18], as is the focus of this paper. The simulations were performed using the PimpleFoam PISO algorithm, and turbulence closure was provided by the $k-\omega$ SST model with the 2003 updated coefficients [19]. The simulated time for each case was 400s, with a time step of 0.03s.

2.2.1. Computational domain

The computational domain was 250 m long, 520 m wide and 43 m tall, corresponding to the height of the ReDAPT site. The domain width was set to achieve a small geometric blockage ratio (ratio of rotor swept area to channel cross-sectional area) of 1.14 %. A vertical flow profile was imposed at the inlet of the computational domain using the atmospheric boundary layer inlet condition available in OpenFOAM. A no-slip wall boundary condition at the bottom of the domain and a stress boundary condition at the top sustained the flow profile. At the outlet boundary, the static pressure was set to a fixed value of 0 Pa, and zero gradient boundary conditions were applied to the turbulence and velocity scalars. Symmetry conditions were applied to the lateral boundaries of the domain. The inflow and top boundary conditions were adjusted to match the flow profile observed from the ReDAPT data [15].

2.2.2. Meshing strategy

The domain was discretised with an Octree mesh to allow a concentration of mesh resolution near the rotor region. The mesh parameters' convergence was evaluated by comparing the simulated flow profile to the field observations and the spanwise distribution of blade forces. A spatially homogeneous grid dimension of 1.5 m was found to capture well the velocity gradients near the seabed and surface boundaries and provide good agreement with field observations of the mean velocity profile.

Two additional levels of grid refinement were employed near the rotor and in the wake region. An intermediate level of resolution of 0.75 m was employed in a region $-0.73d \leq x \leq 1.77d$, $-0.94d \leq y \leq 0.94d$ and $-1d \leq z \leq 0.61d$ around the centre of the rotor, where x is the streamwise coordinate, y is the cross-stream coordinate, and z is the vertical coordinate. The rotor region was further refined with a homogeneous dimension of 0.1875 m in a region $-0.18d \leq x \leq 1.44d$, $-0.67d \leq y \leq 0.67d$, $-0.67d \leq z \leq 0.61d$. The final mesh contained approximately 2.8×10^6 elements.

The actuator line method represents the turbine blades (detailed below). The actuator lines are swept through the static mesh. Thus, no rotating sub-domains or mesh interfaces are required, as would be typical for blade-resolved models. This represents a significant saving in computational cost. However, as described above, it should be noted that the mesh is refined close to the turbine to resolve the large velocity gradients around the blades, as can be appreciated in Fig. 2.

2.2.3. Actuator line model

The turbine was represented using the actuator line method of Sørensen & Shen [20] implemented in OpenFOAM as a user-defined shared object library. Rather than directly meshing the blade geometry, the actuator line model represents the rotor blades virtually by imposing the blade forces on the simulated flow along lines that rotate through the mesh. Each line corresponds to a blade. The actuator forces, therefore, represent an additional term in the momentum equations. The in-house model has been extensively validated against several reference turbines; see, for example, [21,22].

The blade forces are calculated using 2D blade element theory at 100 collocation points distributed sinusoidally along the blade length in order to capture the changes in forces in the root and tip regions of the blades. The lift and drag data that were employed are described in Section 2.3. The flow field around each blade was sampled using the potential flow equivalence method proposed by Ref. [21], and reimposed on the flow using the Gaussian smearing technique of Sørensen & Shen [20]. The calculated blade forces were modified by the tip loss model of Shen et al. [23] to account for the 3D flow effects that reduce the blade forces near the tips.

The turbine nacelle, radius $R_{hub} = 1.35$ m, was represented using a cell-blocking method following [24]. This method blocks fluxes into cells by applying a sufficiently large body force to the selected cells, thus enforcing the velocity to be zero, allowing impermeable bodies to be represented in the numerical domain without requiring the geometry to be resolved explicitly.

2.3. Blade data

2.3.1. General information

The blade is part of the DeepGen tidal project and was designed by Tidal Generation Limited (TGL) and manufactured by Aviation Enterprises Limited. The final blade design report was issued in 2008, and the company responsible for the blade design no longer exists. The rights were bought by another company (Airborne), but some design documents were lost and not provided to FastBlade before testing. The blade was taken from the decommissioned 500 kW tidal stream turbine, previously installed at EMEC's grid-connected test site at the Fall of Warness.

2.3.2. Geometry

The blade length is 5.25 m and the blade cross-section is defined by the NACA 63-4XX aerofoil series, with XX representing the section thickness-to-chord ratio. The thickness-to-chord ratio decreased from 55 % near the blade root to a minimum of 18 % at the tip. The innermost portion of the blade was taken to have a cylindrical cross-section with an

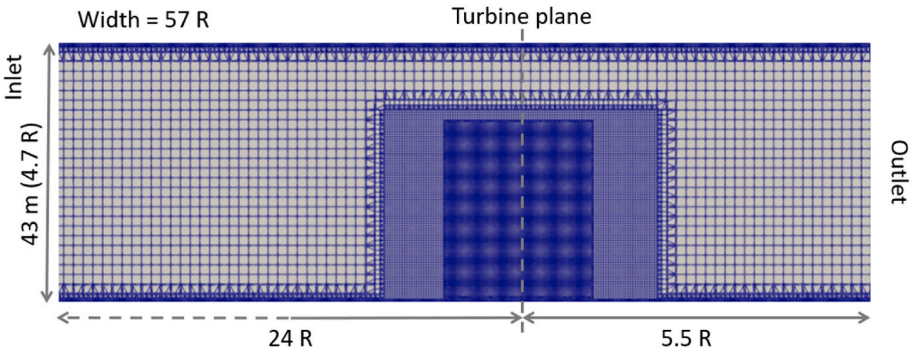

Fig. 2. Technical Drawing Octree mesh used in the CFD.

implied thickness-to-chord ratio of 100 %.

NACA aerofoil coordinates were determined following [25], with the geometry sampled at 300 equally-spaced points. Aerofoil lift and drag characteristics as a function of angle of attack α were computed using QBlade with the chord-based Reynolds number in the range 10E6 < Re < 18E6 The critical number $N_{\text{crit}} = 9$ for all cases.

2.3.3. *Structure*

The entire blade is covered with an 8 mm thick glass fibre skin manufactured using ±45° unidirectional glass fibre prepreg. The general blade structure is presented in Fig. 3; please note that the technical details on the figure have been removed or blurred as requested by the blade owner.The dashed lines in Fig. 3 perpendicular to the blade span represent the locations of pairs of 3 mm thick glass fibre ribs used to stiffen the blade. They allow pressure transfer from the blade skins to the spar caps and are manufactured using ±45° glass fibre unidirectional prepreg. The spar cap is manufactured using 75 % unidirectional carbon fibre epoxy prepreg, with the remaining 20 % containing 90° fibres to improve the transverse strength and stiffness of the spar region. The shear webs are designed to resist the blade's flapwise shear loads and torsional bending, and they are manufactured using ±45° carbon fibre epoxy prepreg. Finally, a rear glass fibre epoxy spar connects the suction and pressure sides 100 mm away from the trailing edge to relieve the trailing edge joint from peel stresses [26].

3. Experimentation

Once the loads were defined, the mechanical test campaign followed the IEC TS 62600–3:2020 standard, performed in the following test sequence: 1st, total mass and centre of gravity; 2nd, natural frequency (3 repeats); 3rd, static test; 4th, natural frequency (3 repeats); 5th, fatigue test; 6th, natural frequency test (3 repeats); 7th, static test; 8th, natural frequency (3 repeats).

3.1. *FastBlade facility description*

FastBlade features a 70-tonne reaction frame capable of resisting high loads during static and fatigue testing (see Table 2.), combined with 880 L per minute of reversible hydraulic flow.

3.1.1. *FastBlade frame*

The reaction frame supports all test specimens and loads (see Fig. 4). It consists of a reaction plane, support wall, T-Slot bed plates and adapter plate, all mounted-on bridge bearings. The reaction frame is in a pit in the floor (2.5 m deep) with the top surface of the reaction plane level with the foundation of the building.

Table 1
Standard deviation in simulated flow speed across the rotor plane in flood and ebb tides as a function of hub-height flow speed.

Flow speed bin [m s^{-1}] at Hub-height	Ebb tide	Flood tide
0.7	0.0429	0.0639
1.4	0.0944	0.1546
2.1	0.1889	0.2257
2.8	0.2782	0.2866
3.0	0.2833	0.3123
3.5	0.3331	–

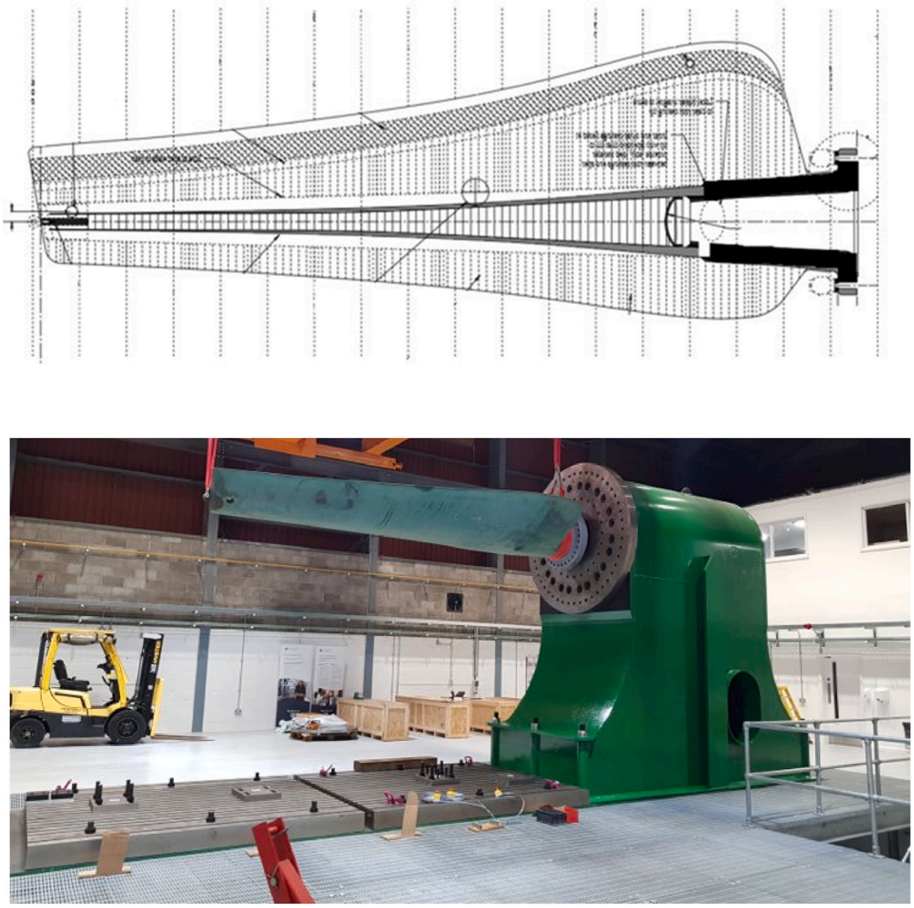

Fig. 3. *Technical Drawing of the Test Blade Looking from the Top View* [26] *and the original blade.*

Table 2
Strong wall load capacities.

Load Capacity	Moment (MN-m)	Shear (MN)
FATIGUE (Up to 400 million cycles Pushing)	4.70	0.94
FATIGUE (Up to 400 million cycles Pulling)	4.70	0.94
STATIC (Assuming quasi-static loading Pulling)	11.96	2.39
STATIC (Assuming quasi-static loading Pushing)	10.74	2.13

3.1.2. *FastBlade hydraulic system*

FastBlade employs 4 Digital Displacement hydraulic reverse pumps developed by Danfoss (see Fig. 5). The ability of the pumps to work in reverse flow flux allows them to recover the energy used during the test. First, an amount of energy is used to apply a load to the specimen producing a deformation of the same. Once the target load is achieved, no more power is added to the system. The pumps then run in reverse, now powered by the weight and spring-back of the specimen, generating energy that can be used to power the pump motor in the next cycle. This system allows FastBlade to operate with up to 80 % less energy used than similar-sized hydraulic systems. Moreover, the pumps also provide all the control of the actuators, meaning that we can avoid the cost of expensive servo hydraulics, nevertheless, this introduces a serious of challenges in the control of the load (see section 4.7).

3.1.3. *Data collection*

For this test campaign, we collected data from both the blade specimen and the FastBlade system. All sensors were calibrated before the experimental campaign, the appropriate sensors were zeroed, and reference measures (“zero readings”) were taken before each test. The data acquisition system used a 4x NI cDAQ 9189 chassis synchronised using a time-sensitive network to provide a reliable distributed logging system. Various C-Series modules are used with the chassis for logging the different signal types. All the data logging is controlled via Flexlogger software, which allows the visualisation and logging of all signals during a test. The control is carried out on a real-time NI controller (NI cRIO 9049), which shares the load signals so that both the test control and logging system can access the load cell data. At the same time, based on the load cell data, the control system sends the signal to the digital displacement hydraulic pumps.

3.1.3.1. Sensor. For this test campaign, the sensors used are described in Table 3, where the last three columns refer to the sensors mounted on the blade, the sensors on the FastBlade system, and the number of sensors the facility can handle, respectively.

In Fig. 6(a) are described using a coordinate system which references lines projected onto the blade surface. The longitudinal lines run between the centre of the root connection to the centre of the lifting eye connection at the blade tip. The crosswise coordinates on the blade are defined as projected lines wrapping around the blade at set distances away from and parallel to the root connection. Crosswise, line 1 is located 900 mm from the root; all other lines after that are equally spaced at 800 mm intervals towards the blade tip. The sensor coordinates are defined using the crosswise line they are on first, followed by the longitudinal line they are on.

Moreover, the blade was monitored using Digital Image Correlation (DIC) equipment. Two sets of stereo-pair cameras were used to capture different regions of the blade. The first set was positioned approximately 4 m away from the blade using 12 mm lenses to capture the entire

Fig. 5. FastBlade’s Digital Displacement hydraulic pumps.

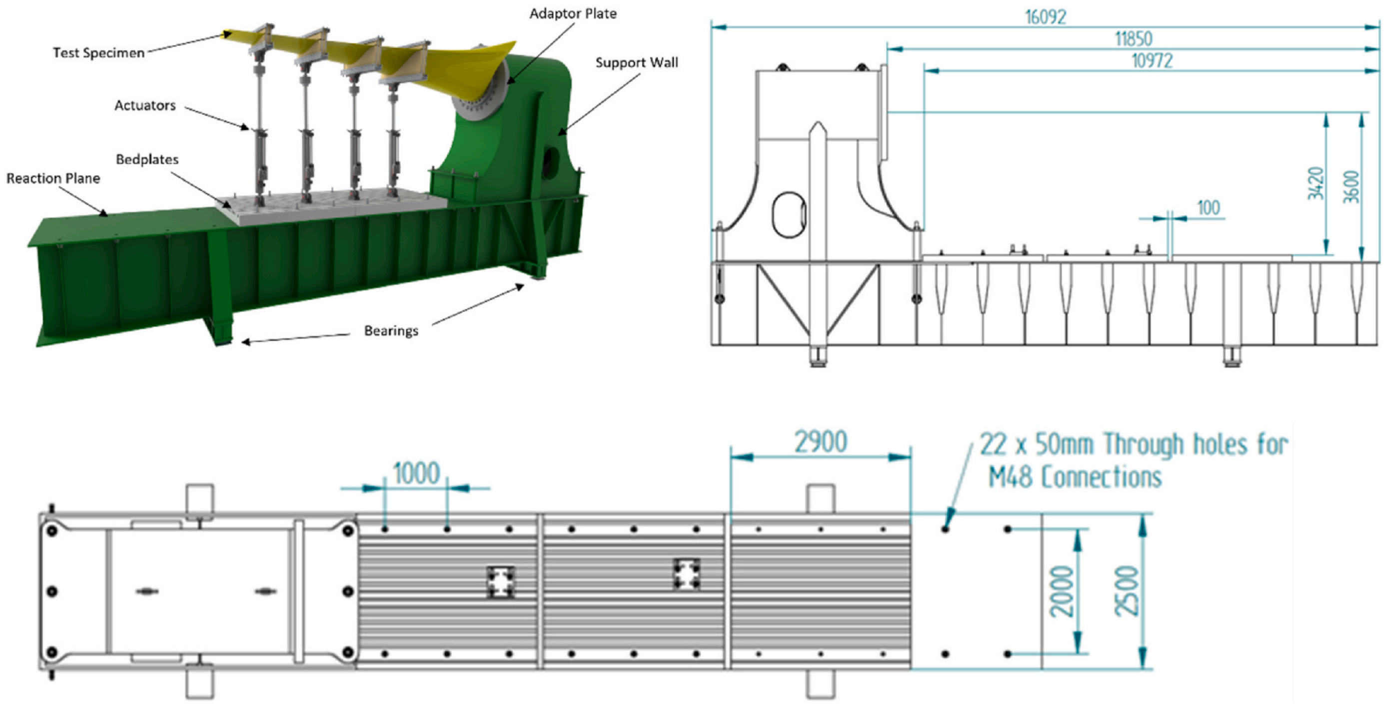

Fig. 4. Reaction frame general arrangement (Top right-hand reaction frame with the specimen, top left-hand lateral section, bottom horizontal section).

Table 3
List of sensors used.

Sensor	Measurement Range	Accuracy/Non-linearity	No. Blade	No. FastBlade	Capacity
Load cell	±500 kN	±0.05 %	1	4	4
Load cell	±25 kN	±0.001 % FS	0	1	1
Accelerometer	±10 G	<3 % FS	0	4	4
Accelerometer	±6 G	<3 % FS	10	0	10
Linear Position	0–1000 mm	±0.02 % FS	4	0	4
Strain Gauge Linear	Strain Limit 5 %		6 × 350Ω	6 × 350Ω	44 × 350Ω
Strain Gauge Rosette	Strain Limit 3 %		16 × 120Ω	0	16 × 120Ω
Thermocouple	−200 to 1260 °C		10	12	32
Linear String Potentiometer	2000 mm	±0.1 %	2	0	2

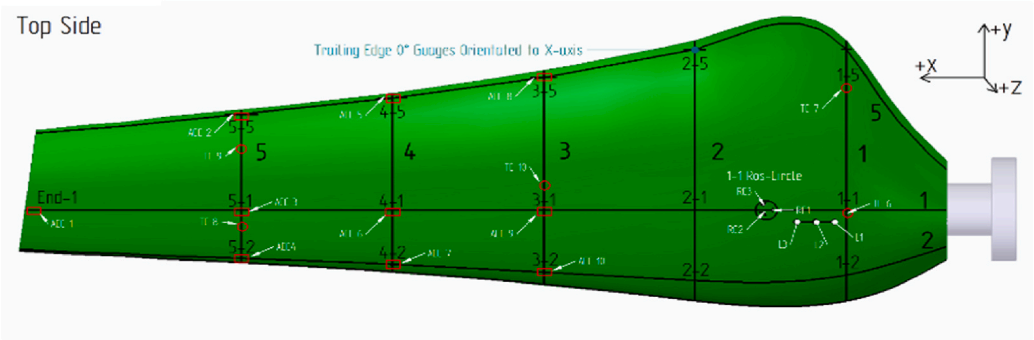

(a) Sensor locations on the top side of the blade.

(b) Coordinate system for blade loads. *(c) Final set up on the reaction frame.*

Fig. 6. Sensor locations (top), blade coordinate system (bottom left) and coordinate system on the reaction frame (bottom right).

surface of the blade between the root connection and the saddle. The second set of cameras was focused on a much smaller blade area at the transition from the metal hub connection to full composite, approximately 800 mm from the root.

3.2 Set up.

The loading direction was based on the documentation available in the Extreme and Fatigue Load Calculations for Deepgen 500 kW Tidal Turbine [27], which describes the axis systems for the blade (see Fig. 6 (a)).In Fig. 6 (b) the coordinate system of the blade and the rotor are presented together, where ZB is the axis extending radially along the blade axis, and YB is perpendicular to the shaft axis, which is assumed to be parallel to the tidal flow; therefore, this becomes the horizontal axis (see Fig. 6 (c)) during the test. XB is perpendicular to YB. Based on the static and fatigue loads and considering both loading in the XB and YB directions, the optimal loading direction is 14.58° anti-clockwise from the XB and actuator distance from the root is 3.55m. This configuration directs 97 % of the load in the XBB direction (edgewise), and 26 % into the YBB direction (flapwise).

Two different methods were tested to apply the loads to the blade. Firstly, an articulated pad system was used (see Fig. 7 (a)). This system would not introduce additional bending moments to the specimen; nevertheless, some pad slippage was observed for over 100 mm in the Y direction towards the trailing edge. The second load introduction method was a clamped wooden saddle with a steel surrounding frame and a 1.5 mm thick silicone sheet at the blade interface. Even if the second system adds additional bending on the blade it would not be sufficient to affect the failure mode of a full-scale tidal blade.

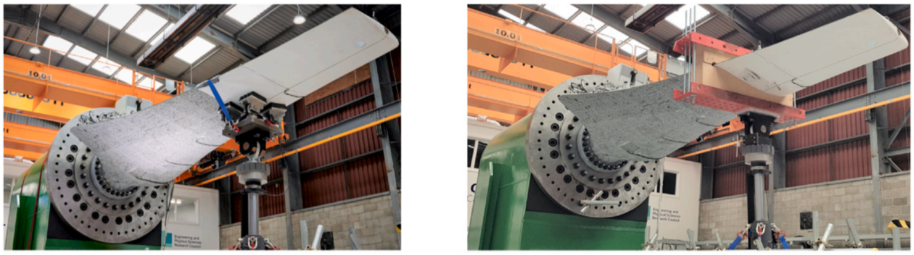

(a)Articulated pad.

(b) Clamping system.

Fig. 7. Load introduction system.

4. Results

4.1. FastBlade's reaction frame performance

To quantify the stiffness of the reaction frame, a laser was used. The laser was mounted on the strong wall and pointed towards the far wall of the test hall. After applying a 200 kN load to the blade, the angle change of the strong wall was calculated to be 0.00286°. At this load, the tip deflection of the blade was 82 mm. The angle change of the strong wall contributed to 0.26 mm of this deflection (0.32 %). This is below the 1 % threshold, as stated in the PD IEC TS 62600–3:2020 A.9.4 [9]; thus, it can be ignored.

4.3. Blade centre of gravity

The centre of gravity is 900 ± 30 mm from the blade's root. It is defined as the intersection of the blade and a vertical line from the crane hook when the blade is aligned at 90° from that vertical line. Simultaneously, the weight of the blade was obtained with an average value of 1588.59 kg (15584.07 N).

4.2. Simulated blade loads

The rotor was simulated in flood and ebb tides across the range of flow speeds indicated in Table 1. The turbine is designed to achieve rated power at a hub-height flow speed of 2.8 ms^{-1}, with a rotational speed of 13.78 rpm, implying an optimal tip speed ratio of $\lambda = R\Omega / U = 4.64$. This was maintained by adjusting the rotor speed for other upstream flow speeds. The rotor occupies a substantial proportion of the 43 m water depth at the site, and consequently, differences in rotor loads and performance were observed due to the different velocity shear profiles between the flood and ebb tides, even for the same hub-height velocity. Specifically, a slightly greater shear was observed across the rotor-swept area in the flood tide compared to the ebb tide.

The spanwise axial and tangential blade loads are shown in Fig. 8, highlighting the mean, minimum and maximum loading profiles during a rotation. The minimum and maximum distributions have been selected based on the forces per unit span at the r/R = 0.9 location, which corresponds approximately to the location where the largest forces are encountered on the blade. Loads generally increase along the blade as a result of the increasing incident flow speed, driven by the rotational component of velocity. A negligible tangential force (contributing to rotor torque) is observed for r/R < 0.35 due to the blending of the blade into the cylindrical root section in this region.

The sheared flow profile encountered by the rotor means that the mean blade loads are slightly higher for the rotor in the ebb tide than the flood tide due to two principal reasons. Firstly, the greater velocity shear across the rotor in the flood tide means that the mass flux through the rotor swept area is slightly lower than that for the ebb tide, for a given hub-height flow speed. This effect is more significant for higher flow speeds. Secondly, greater variation in flow speed through the rotor swept area results in the rotor operating further from its hydrodynamic optimum, which is seen as the increased minimum-maximum spread in blade loads. This has a greater impact on the blade in the lower part of the rotation due to the greater shear in this region, whereas the difference in velocity was less pronounced in the higher part of the water column.

The simulations reproduced 1p and 3p fluctuations in blade loads and overall power and thrust as a result of the rotational sampling of the shear profile by the blades, which also resulted in azimuthal variations

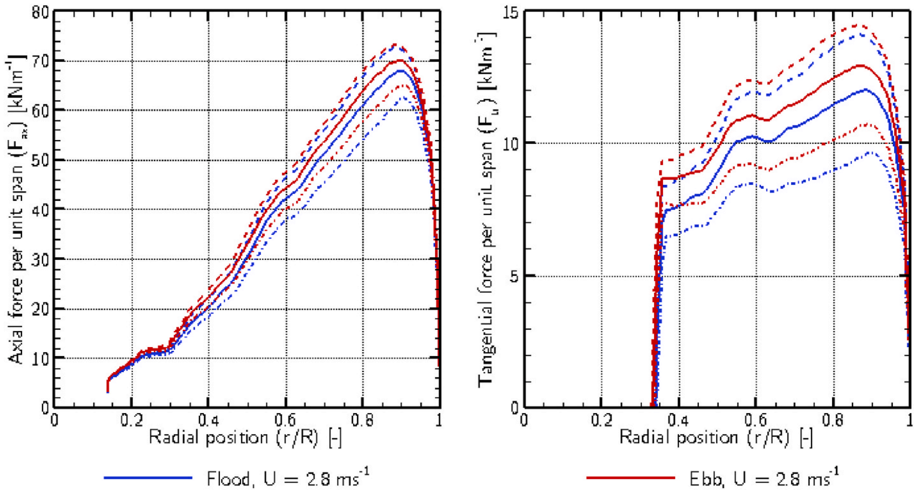

Fig. 8. Spanwise variation in axial (left) and tangential (right) force along a blade in the flood (blue) and ebb (red) tides at a hub-height flow speed of 2.8 ms^{-1}. The mean load over a rotation is indicated with a solid line, with dashed and dash-dot lines use.

in blade root bending moments (RBM) shown in Fig. 9. The results are normalised on the respective means of the flood and ebb flapwise and edgewise (630 kN m and 168 kN m) RBMs in order to highlight the azimuthal variations in loads. Normalised RBMs were generally higher for the rotor operating in the ebb tide between 90 and 270° due to the reduced shear (higher flow speeds) in that case, counterbalanced by the higher flood RBMs in the upper-half of the blade rotation.

While the magnitude of the flapwise RBMs was larger than that for the edgewise direction, the relative variation in the edgewise RBMs was greater as a result of the greater sensitivity to the angle of attack of the flow onto the blade. Additionally, the maximum and minimum RBMs were not encountered at the top- and bottom-dead centre (0° and 180°, respectively), but slightly offset from these positions by about 30°. The rotor-induced swirl velocity interacts with the shear profile to alter the flow incident on the rotor, and due to the different sensitivities of the flapwise and edgewise directions to changes in the angle of attack, the minima and maxima occur at slightly different azimuthal positions.

4.4. Natural frequency

The natural frequency tests show a slight reduction from 18.03 Hz before the test campaign began to 17.93 Hz at the end of the campaign. This reduction of 0.54 % concerning the original value suggests minor damage to the blade. Three measures were made on each natural frequency test, and due to a change in the test process from moving to a clamp-on saddle, the post-fatigue test was carried out with the saddle in place, so it is not comparable with the initial tests. A final test at the end was carried out without the saddle attached to the blade to compare the initial tests. These results are summarised in Table 4.

Table 4
The result from Natural Frequency.

Test	Natural Frequency (Hz)	Standard Deviation	Saddle Attached
Pre-Campaign	18.03	0.006	NO
Post-Static 1	18.00	0.004	NO
Post Fatigue	14.82	0.005	YES
Post-Static 2	14.79	0.002	YES
Post-Campaign	17.93	0.003	NO

4.5. Static loading

Two different static tests were performed, corresponding to tests three (first static test) and seven (second static test), for both cases; the target load was 273 kN, introduced in 120 s, sustained for 3600 s and unloaded in 120 s, following the guidance of the IEC 62600-3 standard [9]. Fig. 10 (a) shows that as the test progresses, the displacement of the blade's tip increases from 120.5 mm to almost 126 mm. This increase in displacement over time would typically indicate a decrease in stiffness from damage to the blade. However, due to the saddle slipping during the test, which altered the loading conditions, we cannot attribute the increase in displacement to damage in the blade. Fig. 10 (b) shows the results of the tip displacement after the second static tests and using the clamping system, which produces a more stable response in comparison to the first test. The load variations are due to possible changes in stiffness of the blade and the control system adjusting to these changes, as well as a faster load transmission between the blade and the new clamping system. Nevertheless, the blade tip displacement variation during the second static test was reduced to 2 mm at the end of the test compared to a 5 mm variation from the first static test.

Damage has likely occurred between the tests, but the change in the saddle makes it challenging to be sure of the source of the observed variations. A comparison between the average strain in the initial and final static tests reveals that, in most cases, the strain values were reduced slightly, as seen in Fig. 11. In the same figure, it can also be appreciated that the DIC strain captures the same trends in the strain as the rosette gauges, showing the same increases and drops along and strain values very similar to those measured by the gauges. Therefore, the DIC system can be reliably used close to regions where the data can be validated using the strain gauges.

4.6. Fatigue

Following the hydrodynamic results, the measured ocean data was extended to a year using harmonic analysis with the python package pytides 0.0.4, giving the mean flow velocity for ebb and flood of 2.8 m/s; which is in concordance to the turbine design (see section 4.2) this value is considered a representative approximation of all the tidal variations across seasons and years. This allows us to define the most common bending moment at the root with a magnitude of 652 kN m. At the same actuator position as the static test, this gives a target load of 184 kN.

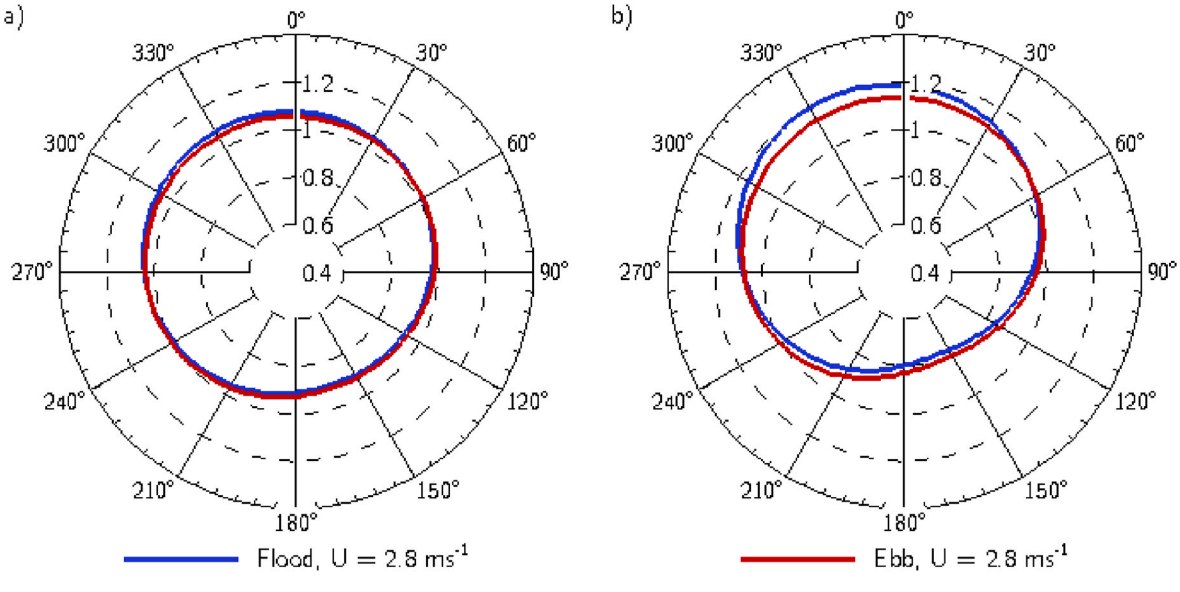

Fig. 9. Azimuthal variation in blade root bending moments in the flapwise (left) and edgewise (right) directions for the flood (blue) and ebb (red) tides at a hub-height flow speed of U = 2.8 ms^{-1}. The bending moments have been normalised on their respective mean.

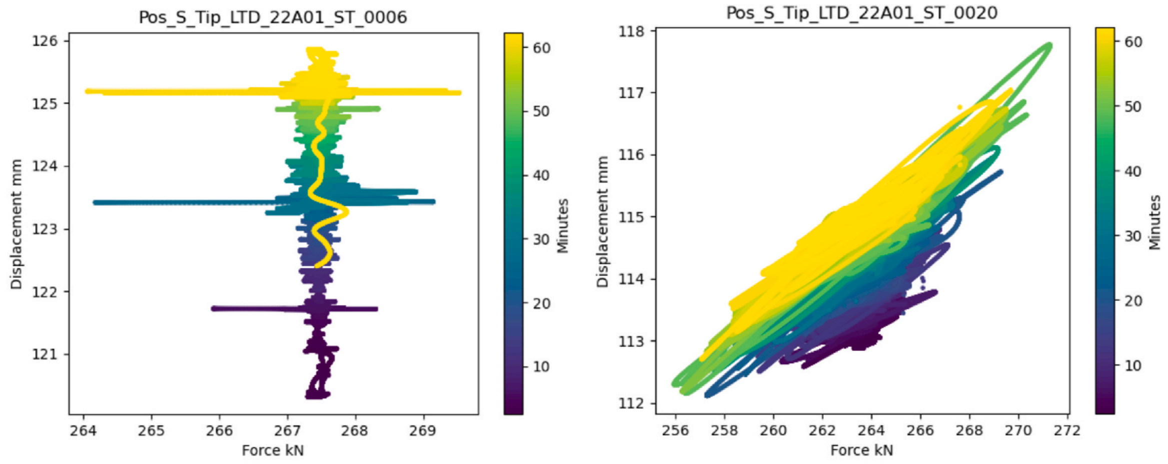

a) First static test

b) Second static test

Fig. 10. Blade tip displacement vs force over time.

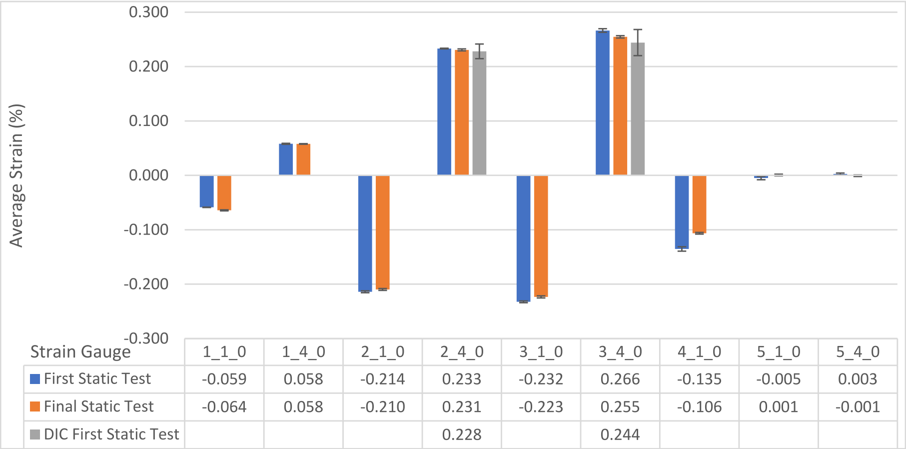

Strain Gauge	1_1_0	1_4_0	2_1_0	2_4_0	3_1_0	3_4_0	4_1_0	5_1_0	5_4_0
🟦 First Static Test	-0.059	0.058	-0.214	0.233	-0.232	0.266	-0.135	-0.005	0.003
🟧 Final Static Test	-0.064	0.058	-0.210	0.231	-0.223	0.255	-0.106	0.001	-0.001
⬜ DIC First Static Test				0.228		0.244			

Fig. 11. Strain comparison during static tests.

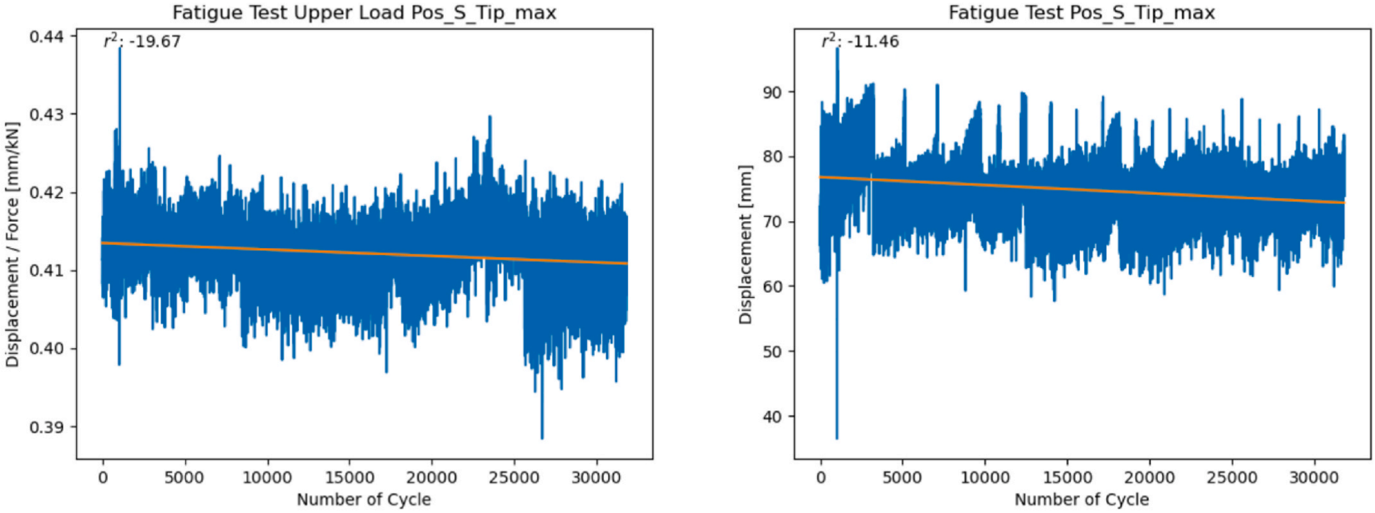

(a) Blade tip Displacement/Force variations.

(b) Maximum tip displacement during the fatigue test.

Fig. 12. Tip Displacement of Blades in Fatigue Loading at peak loads.

During the fatigue test, 31,775 cycles were completed. Under the ocean, the blade will experience two high and two low tides every 24 h and 50 min; based on this, 31,775 cycles represent 22.52 years, of tidal cycles at 1 Hz. It is worth mentioning that these cycles do not consider the RMB variations due to the rotation of the blades (see Fig. 9).

During the test, the mean value of the maximum force per cycle was 182 kN with a standard deviation of 9.8 kN, a minimum peak value of 92 kN and a maximum value of 229 kN. The R value during the fatigue test had an average value of 0.14, a standard deviation of 0.05, and maximum and minimum values of 0.4 and 0.03, respectively, were reached during the test.

Fig. 12 (a) presents the relationship between the tip displacement and force applied during the test campaign. A slight downward trend can be observed, which might indicate an increase in blade stiffness, but it is too subtle a change from which to draw any definitive conclusions. It is interesting to see a significant drop in tip displacement between 20,000 and 25,000 cycles, which might indicate a drastic change in stiffness. Additional testing and analysis will be required to draw any conclusion. Fig. 12 (b) shows that the maximum displacement reduces over time throughout the blade test. The displacement at the tip during the peak of each cycle have an average value of 74.8 mm with a standard deviation of 3.7 mm the minimum value during peak loads was 36.4 mm, and the maximum displacement during peak loads was 96.6 mm. Moreover, to overcome the differences on the maximum peak load, we introduce the relation maximum peak tip displacement to the maximum peak load. For the fatigue test, this relation has a mean value 0.41 mm/kN, standard deviation 0.004 mm/kN, minimum value 0.39 mm/kN and a maximum value of 0.44 mm/kN.

Fig. 13 indicates that the magnitude of the strain in the blade increased (i.e. larger compression strain) throughout the test at equivalent loads. This suggests that the blade at this location (1_1_0) has reduced its stiffness. Fig. 13 also indicates this with the downward trending line. Similar behaviour is seen at locations 3_1_0 (see Fig. 14) and 3_4_0 (see Fig. 15). Moreover, since these two strain gauges are at exactly the same axial location but one on the top and one on the bottom of the blade, and the results are almost a mirror of one to the other.

The mean, standard deviation, maximum and minimum values for the strain gauge represent in Fig. 13(a)–. 14 (a) and Fig. 15 (a)) are shown in Table 5. Due to the variations on the peak loads, we introduce the relationship between strain and force during the peaks of each cycle for which the statistic can be seen in Table 6.

4.7. Test evaluation

Overall, the test is considered successful, nevertheless, during the initial static test the saddle experienced some movement. This resulted in the load not being applied to the same location throughout the test. This was solved by changing from a pad to a clamping system. The PID control is based on a target load, and is managed based on the feedback of the load cell located between the specimen and the actuator. During the fatigue test, the PID control system struggles during a couple of cycles since tuning is required during the test under changing conditions (i.e., change in the properties of the specimen) or due to delays in the communication between the load cell and the control system. This resulted in load cycles which either overshot or undershot target loads during tuningThe modification of the clamping system effectively addressed the slipping encountered during testing. However, it introduced a set of complexities, notably the transition to a stiffer material for the clamping system. This change may result in a more immediate and direct interaction between the blade and the hydraulic system, as the softer cushioning provided by the previous material is absent. Consequently, this could lead to accelerated responses within the control system, potentially resulting in increased load variations. The hydraulic system can input a minimum of 7 cc of oil in order to increase system pressure and thus load. This results in the slight pulsation throughout the static loading. In future tests, this was solved by reducing system stiffness, introducing accumulators into the circuit to smooth out pressure spikes and including flow control valves, which allow a significantly smoother delivery of high-pressure oil into the actuators. Also, more studies need to be made in relation of the possible pre stress that the clamping system can induce.

During the fatigue test, the deviations observed in peak and trough values concerning the desired fatigue waveform are likely attributable to several sources of error. Firstly, the system’s high stiffness renders it highly sensitive to PID tuning adjustments, necessitating manual tuning due to limitations in the resolution of the available autotuning system. Secondly, differences in pump efficiency between pumping and motoring phases require distinct tuning for the upstroke and downstroke of the pistons. However, as the pumping performance is influenced by the motoring stroke and vice versa, achieving independent and complete tuning for each stroke direction proves challenging. Thirdly, the utilization of four pumps, each with varying performance and efficiencies, within a common hydraulic system leads to unpredictable flow paths to and from the pumps, resulting in uncontrollable variations in load.

The temperature of the test hall also varied by up to 10 °C throughout

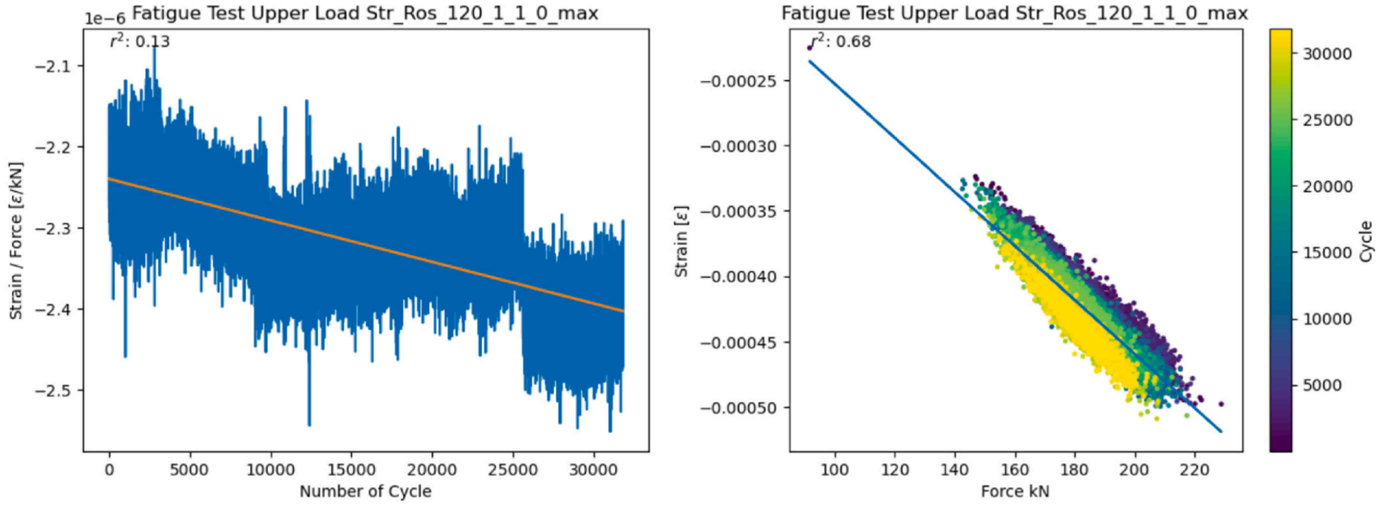

(a) Strain/Force.

(b) Strain vs Load.

Fig. 13. Strain behaviour during a fatigue test at peak loads, blade top surface strain 900 mm from the root.

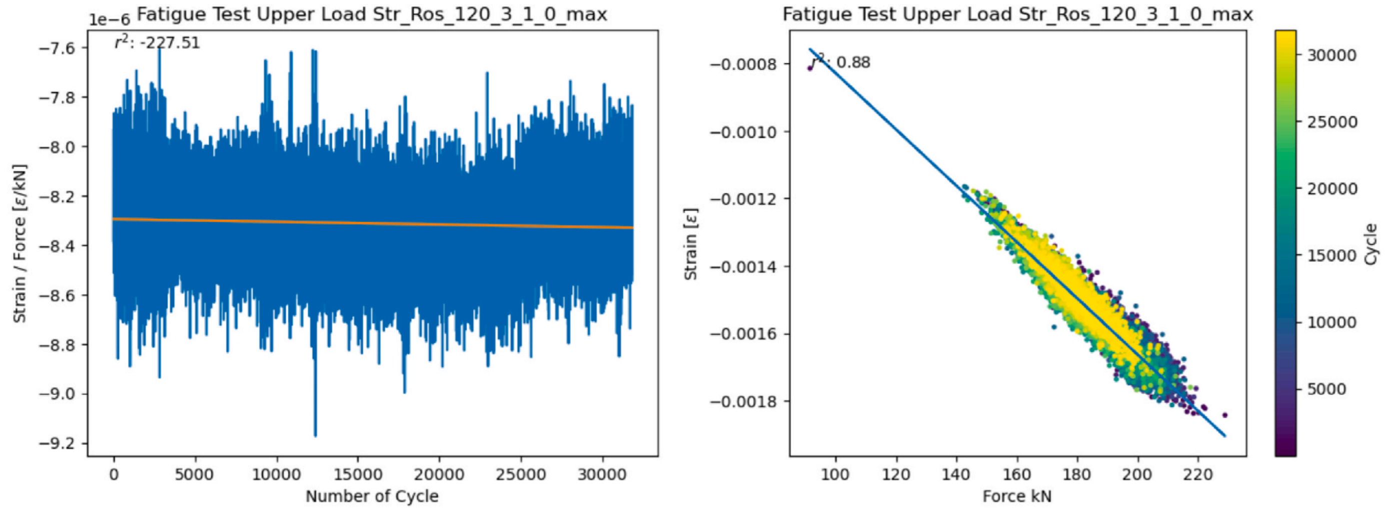

(a) Strain/Force.

(b) Strain vs Load.

Fig. 14. Strain behaviour during a fatigue test at peak loads, blade top surface strain 2500 mm from the root.

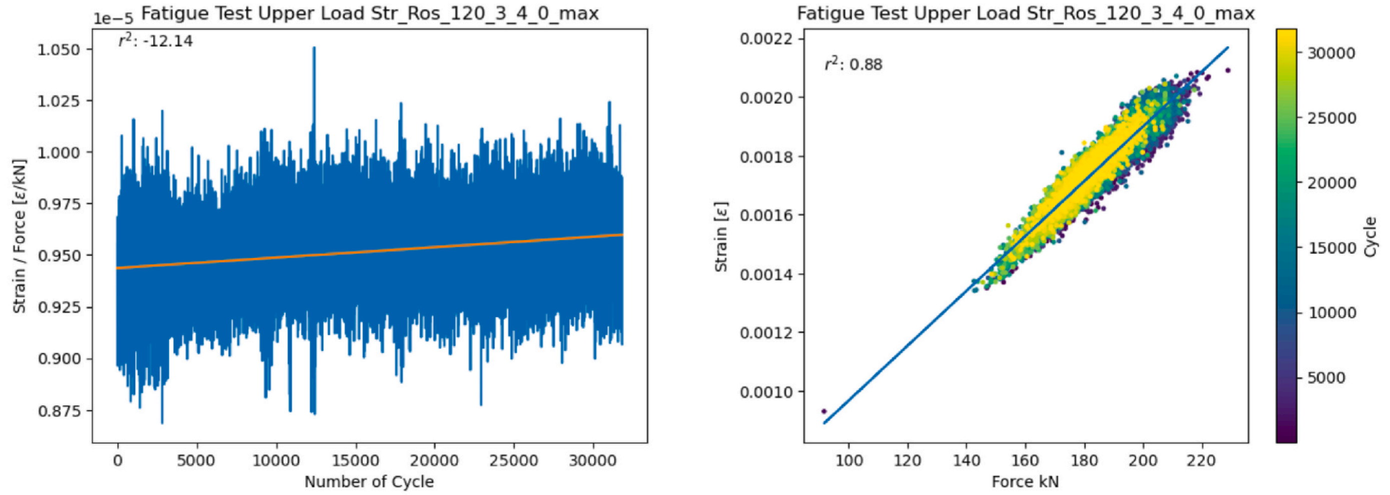

(a) Strain/Force.

(b) Strain vs Load.

Fig. 15. Strain behaviour during a fatigue test at peak loads, blade bottom surface strain 2500 mm from the root.

Table 5
Strain gauge statistics in m/m.

Location	Mean	Standard Deviation	Maximum	Minimum
1_1_0 l	−4.21E-04	2.32E-05	−2.25E-0.4	−5.09E-04
3_1_0	−1.51E-03	8.61E-05	−1.84E-04	−8.15E-04
3_4_0	9.52E-06	−8.15E-04	9.63E-05	2.09E-03

Table 6
Strain gauge statistics in m/m/kN.

Location	Mean	Standard Deviation	Maximum	Minimum
1_1_0 l	−2.32E-06	6.43E-08	−2.08E-06	−2.55E-06
3_1_0	−8.31E-06	1.53 E−07	−7.61E-06	−9.17E-06
3_4_0	1.73E-03	1.75 E−07	1.05E-05	8.68E-06

testing. Where possible, this was considered during the calibration procedures for the strain gauges and other sensors, but the temperature variation during extended test periods could not be accounted for since it implies multiple pauses during the test.

Future tests should incorporate additional fatigue variables, as outlined in section 4.6. Factors such as the rotational movement of the blade (illustrated in Fig. 9) and the influence of turbulence or wave interaction were not accounted for in the current analysis. The rotational effect, particularly pronounced during the flood phase, demonstrates varying magnitudes in both the edgewise and flapwise directions. In the edgewise direction, this effect peaks at 1.16 times the mean RBM, resulting in a RBM delta of 101 kN m, while reaching a minimum of 0.8 times the RBM, generating a RBM delta of 126 kN m. Conversely, in the flapwise direction, the rotational effect achieves a maximum of 1.07 times the mean RBM, resulting in a RBM delta of 11 kN m, with minimum values at 0.9 times the RBM, yielding a RBM delta of 16 kN m. Considering the blade's operational speed of 13.78 rpm and assuming it operates for only half of a flood or ebb cycle, this equates to approximately 7.22E+07 cycles. Thus, even though the test surpasses the 20-year principal tidal load equivalent by an additional 2.52 years or 3554 cycles, it remains insufficient to fully account for the rotational effects.

The load to be replicated for this test campaign is based on the data from the manufacturing company for the static test and the hydrodynamic simulations. The shear stress and bending moments were estimated for different flow conditions for the fatigue test. Since the test was performed with one single actuator, it is evident that there will be limitations to achieving the same spanwise forces and moment distribution. As mentioned in the set-up section, the position at which the load was applied was chosen to minimize the difference between the used and calculated loads; the comparison of the same can be seen in Fig. 16.

Finally, the stiffness variation of the blade during the all-test campaign changes slightly, as seen in Fig. 17. The most notable changes seem to be at the tip; nevertheless, as mentioned, the result from the first static test may not be completely accurate; overall, the stiffness changes seem to be minimal, as shown in Table 7.

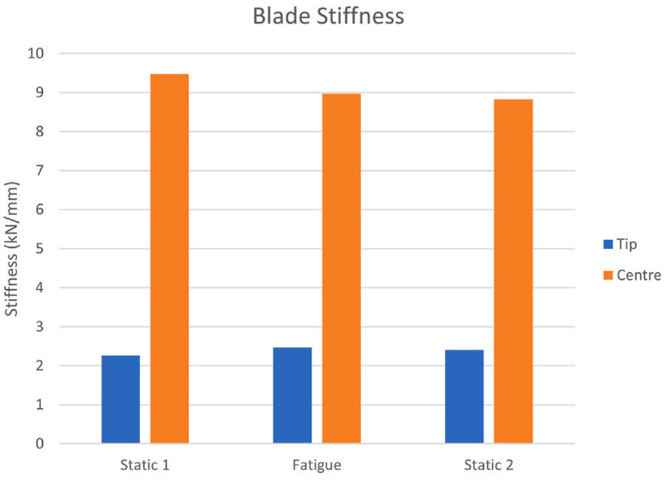

Fig. 17. Blade stiffness variations during the test campaign at the centre and tip.

Table 7
Blade's stiffness variation during the test campaign.

Test	Position	Displacement (mm)	Load (kN)	Stiffness (kN/mm)
Static 1	Tip	120.2	273	2.26
Fatigue	Tip	68.67	169.64	2.47
Static 2	Tip	114.53	276	2.41
Static 1	Centre	28.8	273	9.47
Fatigue	Centre	18.91	170	8.97
Static 2	Centre	31.24	276	8.83

5. Conclusions and future work

This paper demonstrates that the FastBlade fatigue test facility can successfully perform a complete tidal blade mechanical fatigue test, following the available standards. This test campaign allowed the FastBlade team to identify several testing procedure improvements, i.e., control strategies, load introduction, instrumentation layout, instrument calibration, and test design. Finally, the facility opens a series of possibilities to tidal energy developers, designers and researchers due to FastBlade capacity to collect large amounts of data under controlled conditions while replicating many different load scenarios in a fast and economical way.

The blade tested survived the worst-case static load criteria defined by the developer. Moreover, the blade withstood 20 years (equivalent) of the main tidal fatigue loading without catastrophic failure. No specific failures were observed throughout all testing. No audible sounds of failure were detected, nor sudden changes in position or load. The DIC system did not detect any areas of exceptionally raised strain. The highest strain measured with strain gauges was 0.266 % on the bottom surface of the blade, near the loading saddle. All this suggests an over-design on the blade, considering that the blade was under the ocean in working conditions for a few years before the test campaign.

A numerical model of the tested blade will be developed and calibrated using the data of the current experiment campaign. A new test campaign will be carried out in the future, in which a 3-actuator system will be used; this will allow having a more complex load introduced into the blade and compare the results to a more traditional one-actuator system. In a new test campaign, the effect of the saddle clamped to the system will be tracked to detect any possible induced shear stress previous to the test. More sensors will be added to the blade and the FastBlade system (i.e., microphones) to capture more information and evaluate machine learning algorithms to detect any anomaly behaviour.

CRediT authorship contribution statement

Sergio Lopez Dubon: Conceptualization, Data curation, Formal analysis, Investigation, Methodology, Supervision, Validation, Writing – original draft, Writing – review & editing. **Christopher Vogel:** Conceptualization, Data curation, Formal analysis, Funding acquisition, Investigation, Methodology, Writing – original draft, Writing – review & editing. **David Garcia Cava:** Formal analysis, Validation, Writing – original draft, Writing – review & editing. **Fergus Cuthill:** Data curation, Formal analysis, Investigation, Methodology, Validation, Writing – original draft, Writing – review & editing. **Edward D. McCarthy:** Project administration, Resources, Supervision, Writing – original draft, Writing – review & editing, Conceptualization, Formal analysis, Funding

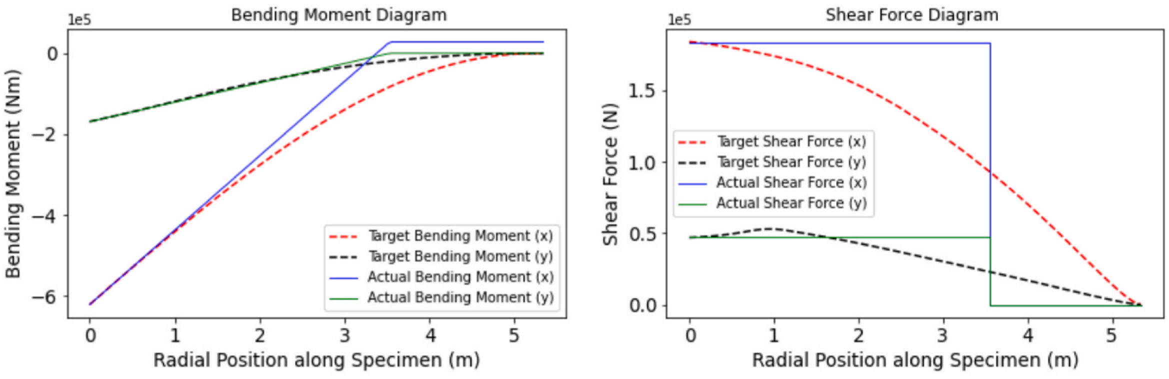

(a) Bending moment.

(b) Shear Force.

Fig. 16. Applied load evaluation.

acquisition, Methodology. **Conchur M. Ó Bradaigh:** Funding acquisition, Supervision, Validation, Writing – original draft, Writing – review & editing.

Declaration of competing interest

The authors declare the following financial interests/personal relationships which may be considered as potential competing interests: Sergio Lopez Dubon reports financial support was provided by European Union's Horizon 2020.

Acknowledgements

First Author: This project has received funding from the European Union's Horizon 2020 research and innovation programme under the Marie Skłodowska-Curie grant agreement No 801215 and the University of Edinburgh Data-Driven Innovation programme, part of the Edinburgh and South East Scotland City Region Deal. All authors: The authors also wish to thank the Supergen ORE Hub for funding received through the Flexible Fund Award FF2020-1063.

References

[1] H. Jeffrey, S. Pennock, P Ruiz-Minguela, D. Cagney, L. Pirttimaa, A European Ocean Energy Industry – the €140bn Economic Opportunity, Indus. Roadmap Ocean Energy, (n.d.). https://www.etipocean.eu/knowledge_hub/industrial-roadmap-for-ocean-energy/(accessed January 13, 2023)..

[2] European Commission, Tidal flows generate huge potential for clean electricity | Res. Innov., (n.d.). https://ec.europa.eu/research-and-innovation/en/projects/success-stories/all/tidal-flows-generate-huge-potential-clean-electricity (accessed January 13, 2023)..

[3] D.M. Grogan, S.B. Leen, C.R. Kennedy, C.M. Ó Brádaigh, Design of composite tidal turbine blades, Renew. Energy 57 (2013) 151–162, https://doi.org/10.1016/j.renene.2013.01.021.

[4] C.R. Kennedy, S.B. Leen, C.M.M.M. Brádaigh, A preliminary design methodology for fatigue life prediction of polymer composites for tidal turbine blades, Proc. Inst. Mech. Eng. Part L J. Mater. Des. Appl. 226 (2012) 203–218, https://doi.org/10.1177/1464420712443330.

[5] C.R. Kennedy, V. Jaksic, S.B. Leen, C.M.Ó. Brádaigh, Fatigue life of pitch- and stall-regulated composite tidal turbine blades, Renew. Energy 121 (2018) 688–699, https://doi.org/10.1016/j.renene.2018.01.085.

[6] W. Li, H. Zhou, H. Liu, Y. Lin, Q. Xu, Review on the blade design technologies of tidal current turbine, Renew. Sustain. Energy Rev. 63 (2016) 414–422, https://doi.org/10.1016/j.rser.2016.05.017.

[7] A. S. Evans, Analysis: Record-low price for UK offshore wind is nine times cheaper than gas - Carbon Brief, (n.d.). https://www.carbonbrief.org/analysis-record-low-price-for-uk-offshore-wind-is-four-times-cheaper-than-gas/(accessed January 13, 2023)..

[8] O. de la Torre, D. Moore, D. Gavigan, J. Goggins, Accelerated life testing study of a novel tidal turbine blade attachment, Int. J. Fatig. 114 (2018) 226–237, https://doi.org/10.1016/J.IJFATIGUE.2018.05.029.

[9] British Standards Institution, Marine energy, Wave, Tidal and Other Water Current Converters. Part 3, Measurement of Mechanical Loads, British Standards Institution, 2020. https://www.document-center.com/standards/show/PD-IEC-62600-3. (Accessed 13 January 2023).

[10] F.R. Cuthill, J.R. Steynor, S.L. Dubon, E.D. Mccarthy, C. Conch, C.M. Bradaigh, J. R. Steynor Is Senior, E.D. Mccarthy, Development of the world's first regenerative hydraulic tidal blade test centre: FASTBLADE, in: Eur. Wave Tidal Energy Conf. 14th EWTEC, 2021. Plymouth, https://proceedings.ewtec.org/product/ewtec-2021-plymouth-uk/. (Accessed 13 January 2023).

[11] C. Glennon, W. Finnegan, N. Kaufmann, Patrick Meier, Y. Jiang, R. Starzmann, J. Goggins, Tidal stream to mainstream: mechanical testing of composite tidal stream blades to de-risk operational design life, J. Ocean Eng. Mar. Energy. 8 (2022) 163–182, https://doi.org/10.1007/s40722-022-00223-4.

[12] N. Caldwell, Review of early work on digital displacement® hydrostatic transmission systems, BATH/ASME 2018 Symp. Fluid Power Motion Control, FPMC 2018, https://doi.org/10.1115/FPMC2018-8922, 2018.

[13] M. Ehsan, W.H.S. Rampen, S.H. Salter, Modeling of digital-displacement pump-motors and their application as hydraulic drives for nonuniform loads, J. Dyn. Syst. Meas. Control. Trans. ASME. 122 (2000) 210–215, https://doi.org/10.1115/1.482444.

[14] W. Rampen, D. Dumnov, J. Taylor, H. Dodson, J. Hutcheson, N. Caldwell, A digital displacement hydrostatic wind-turbine transmission, Int. J. Fluid Power 21 (2021), https://doi.org/10.13052/IJFP1439-9776.2213, 87–112–187–112.

[15] B. Sellar, Metocean Data Set from the ReDAPT Tidal Project: Batch 1, Part 2, 2011-2014, 2017.

[16] B.G. Sellar, TIDAL energy site CHARACTERISATION at the fall of warness, EMEC, UK, Edinburgh. https://redapt.eng.ed.ac.uk/library/eti/reports_updated/TechnicalReportonTidalSiteCharacaterisationDuringtheReDAPTProjectv4.0.pdf, 2016.

[17] B.G. Sellar, G. Wakelam, D.R.J. Sutherland, D.M.I. Id, V. Venugopal, Characterisation of tidal flows at the European marine energy centre in the absence of ocean waves, Energies 11 (2018), https://doi.org/10.3390/en11010176.

[18] U. Ahmed, D.D. Apsley, I. Afgan, T. Stallard, P.K. Stansby, Fluctuating loads on a tidal turbine due to velocity shear and turbulence: comparison of CFD with field data, Renew. Energy 112 (2017) 235–246, https://doi.org/10.1016/J.RENENE.2017.05.048.

[19] F.R. Menter, M. Kuntz, R. Langtry, Ten years of industrial experience with the SST turbulence model, turbul, Heat Mass Tran. 4 (2003). http://aaac.larc.nasa.gov/tsab/cfdlarc/aiaa-dpw/. (Accessed 13 January 2023).

[20] J.N. Sørensen, W.Z. Shen, Numerical modeling of wind turbine wakes, J. Fluid Eng. 124 (2002) 393–399, https://doi.org/10.1115/1.1471361.

[21] J. Schluntz, R.H.J.J. Willden, An actuator line method with novel blade flow field coupling based on potential flow equivalence, Wind Energy 18 (2015) 1469–1485, https://doi.org/10.1002/we.1770.

[22] A. Wimshurst, R.H.J. Willden, Analysis of a tip correction factor for horizontal axis turbines, Wind Energy 20 (2017) 1515–1528, https://doi.org/10.1002/WE.2106.

[23] W.Z. Shen, J.N. Sørensen, R. Mikkelsen, Tip loss correction for actuator/Navier–Stokes computations, J. Sol. Energy Eng. 127 (2005) 209–213, https://doi.org/10.1115/1.1850488.

[24] D.D. Apsley, T. Stallard, P.K. Stansby, Actuator-line CFD modelling of tidal-stream turbines in arrays, J. Ocean Eng. Mar. Energy. 4 (2018) 259–271, https://doi.org/10.1007/S40722-018-0120-3/FIGURES/17.

[25] C.L. Larson, C.W. Brooks, A.S.H. Jr, D.W. Sproles, Computer Program to Obtain Ordinates for NACA Airfoils, 1996. Tech Report 4741, Hampton, Virginia, USA, https://ntrs.nasa.gov/api/citations/19970008124/downloads/19970008124.pdf.

[26] C. Huxley-Reynard, J. Thake, G. Gibberd, TG-RE-040-0091 Rev B Deepgen Blade Design Report, 2008. Bristol.

[27] C. Huxley-Reynard, J. King, G. Gibberd, TG-RE-000-0081 Rev D Extreme and Fatigue Load Calculations for Deepgen 500kW Tidal Turbine, 2008. Bristol.